Bioactive Materials 40 (2024) 261–274

Contents lists available at ScienceDirect

Bioactive Materials

journal homepage: www.keaipublishing.com/en/journals/bioactive-materials

Advanced biomedical and electronic dual-function skin patch created through microfluidic-regulated 3D bioprinting

Ting Dong [a], Jie Hu [b], Yue Dong [a], Ziyi Yu [a], Chang Liu [a], Gefei Wang [b,**], Su Chen [a,*]

[a] State Key Laboratory of Materials-Oriented Chemical Engineering, College of Chemical Engineering, Jiangsu Key Laboratory of Fine Chemicals and Functional Polymer Materials, Nanjing Tech University, Nanjing, 210009, China
[b] Department of General Surgery, Affiliated Jinling Hospital, Medical School of Nanjing University, Nanjing, 210002, China

ARTICLE INFO

Keywords:
3D bioprinting
Skin patches
Wound healing
Pressure sensor

ABSTRACT

Artificial skin involves multidisciplinary efforts, including materials science, biology, medicine, and tissue engineering. Recent studies have aimed at creating skins that are multifunctional, intelligent, and capable of regenerating tissue. In this work, we present a specialized 3D printing ink composed of polyurethane and bioactive glass (PU-BG) and prepare dual-function skin patch by microfluidic-regulated 3D bioprinting (MRBP) technique. The MRBP endows the skin patch with a highly controlled microstructure and superior strength. Besides, an asymmetric tri-layer is further constructed, which promotes cell attachment and growth through a dual transport mechanism based on hydrogen bonds and gradient structure from hydrophilic to superhydrophilic. More importantly, by combining the features of biomedical skin with electronic skin (e-skin), we achieved a biomedical and electronic dual-function skin patch. In vivo experiments have shown that this skin patch can enhance hemostasis, resist bacterial growth, stimulate the regeneration of blood vessels, and accelerate the healing process. Meanwhile, it also mimics the sensory functions of natural skin to realize signal detection, where the sensitivity reached up to 5.87 kPa^{-1}, as well as cyclic stability (over 500 cycles), a wide detection range of 0–150 kPa, high pressure resolution of 0.1 % under the pressure of 100 kPa. This work offers a versatile and effective method for creating dual-function skin patches and provide new insights into wound healing and tissue repair, which have significant implications for clinical applications.

1. Introduction

Tissue engineering towards rebuilding new organs or tissue by using various biomedical technologies is highly desirable. Employing biomedical technologies, this field has bifurcated into two pivotal methodologies. The first leverages scaffolds and cells to provide a protective barrier and support skin regeneration in the wake of severe damage, utilizing a suite of biomaterials that are both biocompatible and can be integrated with patient-derived cells [1]. The second method strives to imitate the function of skin through the advancement of electronic skins, integrating artificial intelligence, soft robotics, and wearable tech [2–5]. The development of smart bio-adhesives [6], high-performance soft pressure sensors [7], deformable sensors or functional circuits [8], and stand-alone stretchable sensing platforms (driven by human movement) [9] will provide more comprehensive opportunities to blur the boundaries between the biological and technological domains [10]. However, how to integrate the above two methods to achieve both rapid wound healing and to reproduce the functional properties of the skin is an urgent problem. The emergence of 3D bioprinting offers a versatile, reliable replication of organic functions and structures [1]. When the bioprinting is enhanced by microfluidic technology, it shows distinct advantages of gentle fabrication, high cell viability and precise control over the intricate microarchitecture, paving the way for creating anisotropic tissues and organs with life-like properties. This innovative amalgamation has already shown success in fabricating complex organ structures such as the heart and lung, signifying a groundbreaking shift in tissue engineering and regenerative medicine [5,10,11].

These inks incorporated living cells [1,12], extracellular matrix (ECM) components [1,13], cellular mediators [14], and various

Peer review under responsibility of KeAi Communications Co., Ltd.
* Corresponding author.
** Corresponding author.
E-mail addresses: Gefei_W@163.com (G. Wang), chensu@njtech.edu.cn (S. Chen).

https://doi.org/10.1016/j.bioactmat.2024.06.015
Received 23 March 2024; Received in revised form 6 June 2024; Accepted 7 June 2024

additives [1,15], are all essential for creating viable tissue constructs. For instance, tissue-specific bioinks have been developed by combining natural polymers like alginate with ECM from decellularized tissues, achieving shear thinning and high cell viability [11]. Furthermore, bioinks based on gelatin, alginate, hyaluronic acid, and photoactive derivatives have been used for 3D printed artificial skin patches [16]. Notably, bioactive glass (BG) has emerged as a promising additive for promoting vascular regeneration and tissue repair, owing to its capacity to stimulate growth factor production and enhance cellular functions [17,18]. The main challenge remains to print these materials under gentle conditions while retaining bioactivity and precisely managing the bioactive components. Direct-write 3D printing of fibers, in particular, has been crucial for crafting artificial skin, ensuring scaffold permeability as well as essential wound healing functions [19,20]. Despite significant research into various biomaterials for artificial skin—such as porous foams [21], injectable and self-healing hydrogels [22–24], and nanofiber scaffolds [25–27], controlling the microstructure to optimize permeability and structural variety remains a significant hurdle.

Another indication is the structural design of artificial skin, asymmetric hydrophilic-hydrophobic structure has emerged as a practicable and effective dressing that pumps wound fluids in one direction to accelerate wound healing by mimicking the natural skin's epidermis and dermis structure [28,29]. Specifically, these designs utilize a hydrophilic or superhydrophilic layer to create a surface energy gradient, enhancing fluid absorption, and encouraging cell adhesion and growth. In contrast, the outer hydrophobic layer mimics the natural epidermis, effectively guarding against bacterial contamination and external elements [30]. This dual-layer approach promises to mitigate infection risks and has shown potential for use in wound care. Bao et al.'s four-layer composite with a Janus structure optimize fluid transfer and bioactive ion delivery to promote angiogenesis [31], while Zhang et al.'s bioactive sandwich structured dressing aids in fluid absorption and supports hair follicle and burn wound healing [32]. Yet, challenges persist with the material and structural laws affecting adsorption rates and the mechanical properties of these artificial skins, which currently limit broader application. Especially, methods allowing the function integration, creation of specific microenvironments and precise microstructures are crucial, which will guide the design and construction of functional artificial skin.

In this work, we construct biomedical/electronic dual-function skin patches via microfluidic-regulated 3D bioprinting (MRBP) technique (Fig. 1A). Notably, the MRBP shares distinct advantages of both microfluidic and 3D bioprinting technology. It not only enables preciously control of microstructure and morphology, but also allows mild fabrication process with superiorities of shape fidelity and versatility, and high viability of the encapsulated cells, which is of great significance in tissue engineering, skin and regenerative biological medicine [33,34]. Besides, our approach includes the development of a new bioink composed of polyurethane and bioactive glass (PU-BG), which is not only biocompatible but also could foster cell migration. Our theoretical studies of surface energy gradients aid in understanding blood adsorption and cell migration, which in turn guide the design of skin patch, making it less arbitrary and more functionally consistent. The unique asymmetric structure combining hydrophilic, superhydrophilic, and hydrophobic layers, represented by PU-BG, PU-PAA, and PCL

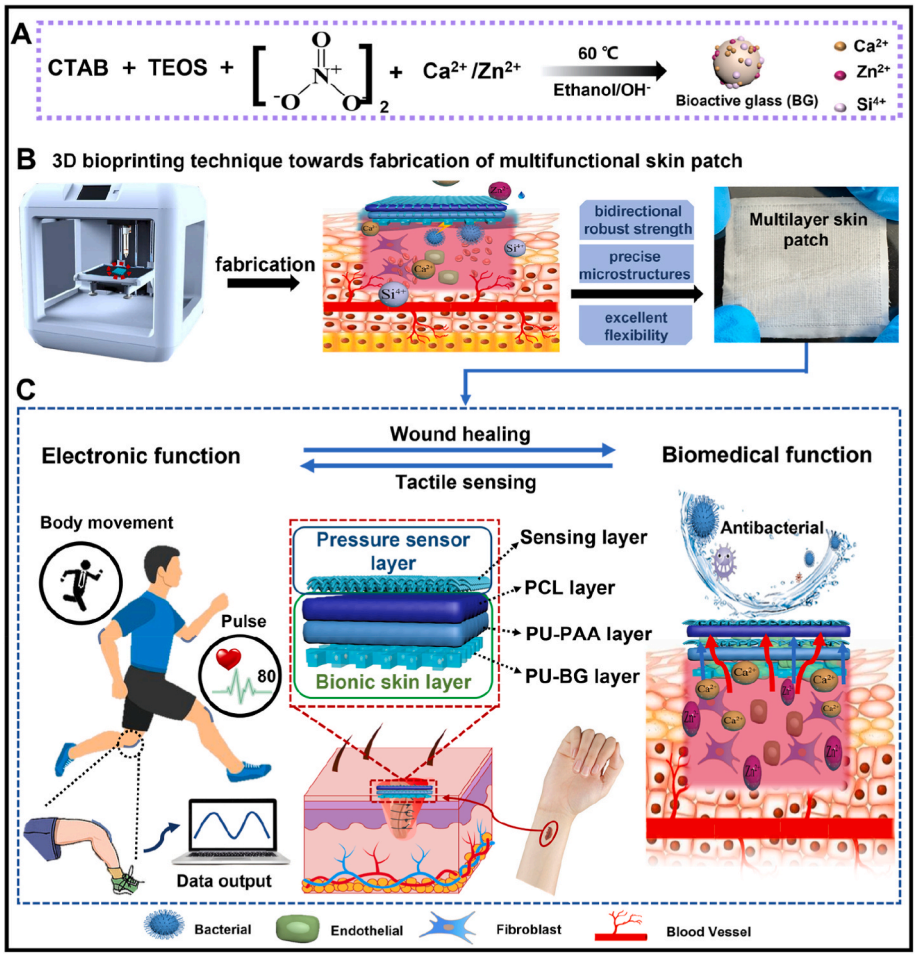

Fig. 1. A. Schematic illustration of the fabrication of biomedical and electronic dual-function skin patches by microfluidic 3D bioprinting technique. **B.** Outstanding features of biomedical and electronic dual-function skin patches, including absorption of wound exudate, inhibition of bacterial infection, accelerated wound healing and signal sensing.

respectively, has been theoretically validated and confirmed through empirical studies [35]. These artificial skin patches not only exhibit excellent biocompatibility, antibacterial properties and mechanical strength, but also enhance the wound healing process, including coagulation, fibroblast activity, angiogenesis, collagen deposition, and tissue regeneration. More importantly, by combining the advantages of electronic skin, a bio/electronic bifunctional skin patch was constructed, which possesses sensory functions of natural skin with the sensitivity of 5.87 $kPa^{-1}$and wide detection range of 0–150 kPa as well as high pressure resolution of 0.1 % under the pressure of 100 kPa, provides antibacterial property, as well as promotes wound healing (Fig. 1B). This advancement provides a new perspective on the design of intelligent, functionally integrated skin patches for clinical wound treatment, opening new avenues for medical-electronic application.

2. Experimental section

2.1. Materials

All chemicals used in this work were commercially available and used without further purification. Polycaprolactone (M_n 60000–65000, PCL) and Polyacrylic acid (M_n 3000000, PAA) were purchased from Sigma-Aldrich Co., Ltd. (USA). Polyurethane (PU) was purchased from Zhejiang Huafon Spandex Co., Ltd. 2,2,2-Trifluoroethanol, N, N-Dimethylformamide (DMF), Zinc nitrate hexahydrate ($Zn(NO_3)_2{\cdot}6H_2O$), Calcium nitrate tetrahydrate ($Ca(NO_3)_2{\cdot}4H_2O$), Ammonia solution, Ethanol (75 %) were purchased from Aladdin Reagent Co., Ltd. (Shanghai, China). Tetraethyl orthosilicate (TEOS) was purchased from Alfa Reagent Co., Ltd. Hexadecyl trimethyl ammonium bromide (CTAB) was purchased from Sinopharm Chemical Reagent Co., Ltd. Deionized (DI) water was used in all the experiments. Mouse L929 cells were purchased from Nanjing Keygen Biotechnology Co., Ltd. (China) and cultured in EMEM (Gibco, USA) with 10 % fetal bovine serum (FBS) (Gibco, USA) and 5 % CO_2 concentration at 37 °C. Live/Dead viability assay kit (KGAF001) for animal cells was purchased from Nanjing Keygen Biotechnology Co., Ltd., (China). *Escherichia coli* and *Staphylococcus aureus* were cultured on a plate medium (Hopebiol Biotech Co., Ltd, China). All male Sprague-Dawley rats (200–250 g) were provided from Jinling Hospital of Nanjing Command (Nanjing, China). The rats were allowed to contact food and water freely at 50 % relative humidity and 26 °C and treated strictly according to the "Guidelines for the Care and Use of Laboratory Animals". All of the animal and experimental procedures were approved by the Animal Investigation Ethics Committee of Jinling Hospital of Nanjing Command.

2.2. Preparation of BG by microfluidic technology

Firstly, 8.37 g of TEOS, 2.5 g of $Zn(NO_3)_2{\cdot}6H_2O$, and 5.0 g of ethanol were added into a 20 mL glass vessel. The mixture was stirred at room temperature until the solid was completely dissolved, defined as solution A. 1.6 g of $Ca(NO_3)_2{\cdot}4H_2O$ was added into 11.2 g of the mixture of TEOS and ethanol (3.1:2.5 in mass ratio) in a 20 mL glass vessel. The mixture was stirred until clarified, defined as solution B. Ammonia water (3.54 g), CTAB (1.5 g), ethanol (120 mL) and DI water (350 mL) were added into a 500 mL glass vessel. The mixture was heated at 60 °C under magnetic stirring until it become transparent, defined as solution C. Then, the three-channel microfluidic chip was designed to prepare BG. The Solution A, B, C prepared above was injected into three separate syringes (connecting with the syringe pumps), respectively. After reaction, the suspended matter was collected, centrifuged at a speed of 8000 rpm/min and washed with DI water for at least three times. Subsequently, the as-prepared BG was placed in the oven to dry for 24 h, followed by calcine in muffle furnace at 600 °C for 6 h to remove the remaining surfactant CTAB. Specially, the feed rate of solution A, B, C was set at 2, 2.5, 40 mL/h, respectively and the product was defined as BG. BG-1 reflects the feed rate of solution A, B, C of 1, 1 and 40 mL/h, respectively. While BG-2 reflects the feed rate of solution A, B, C of 3.2, 2.8 and 40 mL/h, respectively.

2.3. Fabrication of tri-layer multifunctional skin patches

The tri-layer multifunctional skin patches were prepared by a microfluidic electrospin-3D bioprinting machine (Supplementary Fig. S1) (JNS-MS-05-ME01, Nanjing Bell-Time Co., Ltd). Detailed procedure is as follow. i) 1 g of PCL solid was dissolved in 9 g of 2,2,2-trifluoroethanol solution to obtain 10 wt % PCL spinning solution, which was stirred at room temperature for 6 h. ii) 1.0 g of PU and 0.5 g of PAA solids were dissolved in 8.5 g of DMF solution to obtain PU-PAA spinning solution. iii) 1.5 g of PU solids and a certain amount of BG powder were dissolved in 8.5 g of DMF solution. The as-prepared PU-BG solution was directly used for bio-3D printing, and the print path (shape, height, size) was set and finished on the substrate. Then, The PU-PAA and PCL spinning solutions were electrospun in sequence on the PU-BG substrate. Under the positive electrostatic field, the solution was instantly transformed into nanofibers. While under the negative electrostatic field, nanofibers were sequentially adsorbed on the surface of the PU-BG layer to obtain the unique asymmetric three-layer wound dressing patches. The voltage was constant at 15 KV during microfluidic electrospinning process. The whole process was performed at 20 °C and 70 % relative humidity. Finally, the PU-BG/PU-PAA/PCL skin patches were obtained and dried at room temperature for 12 h to remove the residual 2,2,2-trifluoroethanol and DMF.

2.4. Fabrication of biomedicine/electronic difunctional skin patch

The resistive flexible sensing films were purchased from Shenzhen Tonglijian Technology Co., Ltd. The biomedicine/electronic difunctional skin patches were prepared by a microfluidic electrospin-3D bioprinting machine. Firstly, the sensing membrane was fixed, followed by electrospinning PCL and PU-PAA in sequence. Then the PU-BG layer was completed on the PU-PAA surface by 3D printing. The electrospinning and 3D printing procedure is similar to that of section 2.3.

2.5. Ions release behavior of the skin patches

The ion release behavior of BG was studied by placing 5 mg BG nanospheres in 10 g PBS solution at pH of 7.4 and temperature of 37 °C. Then, at the defined time intervals, the solutions were centrifuged at rate of 10000 rpm/min for 30 min and replaced with 10 g fresh PBS solution. The concentrations of Ca, Si and Zn ions in PBS were analyzed by ICP-AES (Thermo Fisher X series 2, USA).

2.6. Cell viability and cytocompatibility of the skin patches

The cell viability and cytocompatibility of skin patches were verified by a live/dead cell viability assay. The L929 cells were plated in six-well plates on the skin patches at a density of 5 × 10^5 cells/well. After cultured with 24 h and 48 h, the culture mediums were carefully removed and then supplemented with calcein-AM solution and PI solution. Samples were washed three times by cold PBS after incubation for another 30 min, and then took images by a fluorescent microscope. All experiments were repeated for three times.

2.7. Water contact angle and air permeability test

The water contact angle of the samples was measured with a contact angle tester (DSA100, KRÜSS, Germany) using 5 μL water droplets. The images were chosen at a specified time. The permeability of the samples was measured using a Capillary Flow Porometer (IPORE-1500AEX-Clam). The differential pressure between the inside and outside of the sample was controlled at 100 Pa, and the test area was 4 cm^2. The tests were conducted randomly at 10 sites for reproducibility.

2.8. Antibacterial activity of the tri-layer skin patches

Escherichia coli and *Staphylococcus aureus* were used to test the antibacterial activity. 5 mL of bacteria solution (10^4 CFU/mL) was cultured with skin patches for 24 h and 48 h at 37 °C. After 24 h and 48 h, the suspension was taken out and seeded on nutrient agar plate to calculate the bacterial colonies. We also spread the bacteria solution evenly on nutrient agar plat and observed the bacteriostasis ring by putting the skin patches onto the agar surface for 24 h and 48 h at 37 °C.

2.9. Hemostatic capability of tri-layer skin patches

We used a mouse liver bleeding model to evaluate the hemostatic effects of the skin patches. All rats were anesthetized with isoflurane. We exposed the rat liver and made a 1 cm length incision with a surgical scalpel. Then, the skin patches were placed on the surface of the liver bleeding site. The liver bleeding condition were calculated.

2.10. Evaluation of wound healing in vivo

We employed the tri-layer skin patches as wound dressing and investigated the wound healing in vivo. Before the surgery, all rats were anesthetized with 4 wt% chloral hydrates through intraperitoneal injection. The dorsum hair of mice was shaved, and the exposed skin was disinfected with 75 % ethanol. The full-thickness round skin wound with a diameter of 2 cm was made with a circular punch. Mice were randomly divided into four groups and treated with PBS, PU-BG, PU-BG/PU-PAA, PU-BG/PU-PAA/PCL, respectively. Wound areas were photographed and measured on days 0, 3, 5, 7 and 14 after surgery. Wound healing rate was calculated as the percentage of the area of the healed wound relative to the original infected wound area. After 14 d, new granulation tissue was removed and the skin tissue was fixed in formaldehyde for histological analysis and immunofluorescence staining.

2.11. Histology and immunofluorescence staining

Granulation tissue samples were removed from neutral formaldehyde, dehydrated, and paraffin-embedded. Slicers were sectioned continuously for 5 μm following standard procedures to produce hematoxylin-eosin staining and immunofluorescence staining. Skin tissue sections were washed with PBS and then incubated with goat serum at room temperature. To assess two typical pro-inflammatory factors, sections were reacted with primary antibodies Anti-IL-6 antibody (ab179570) and Anti-TNF-α antibody (ab183218), then the sections were washed and incubated with fluorescently coupled secondary antibodies Alexa Fluor 555-. For evaluation of neovascularization, sections were incubated with anti-CD31 antibody (Abeam, ab281583) and anti-α smooth muscle actin antibody (Abeam, ab7817). Then sections were incubated with goat anti-rabbit IgG-H&L (Alexa Fluor 647) and goat anti-mouse IgG secondary antibodies (Alexa Fluor 488) (Abeam, ab150117) for 1 h. To assess collagen deposition, sections were incubated with anti-mouse collagen polyclonal primary antibody (Abcam, ab96723) for 2 h at room temperature, followed by the secondary antibody for 1 h, and then counterstained with DAPI. To assess macrophage polarization, sections were incubated with anti-CD68 (Abcam, ab283654) and anti-CD86 (Abcam, ab238468) to label M1 macrophages, anti-CD68 (Abcam, ab283654) and anti-CD206 (Santa Cruz, Sc-34577) to label M2 macrophages. Subsequently, sections were washed and incubated with fluorescently coupled secondary antibodies Alexa Fluor 488- and 555-. DAPI was used as nuclear counterstain. Photographs were obtained and analyzed by Opera Phenix (PerkinElmer Inc., UK).

2.12. Pressure sensing measurements

For pressure sensing, copper foils and electrically conductive silver pastes were used to assist the measurement. The copper foils were connected to a Keithley 2450 digital source meter, and the pressure sensor was installed on the testing board of Mark-10. Cycle stable measurement was also performed by using Mark-10 mechanical test apparatus. The resistance variation was monitored with an LCR meter (UC2831, UCE, China). The normalized current (ΔI/Io) versus the press (kPa) curve was plotted using Origin.

2.13. Water weight loss rate of electronic skin patches

We further sealed a water container by the skin patch to record the weight loss rate of the water inside. The water container was filled with 100.0 g of deionized water. Then the water container was irradiated at a solar light intensity where the water turned into water vapours and produced a white mist above the skin patch. At regular intervals, the weight of the remaining water was recorded. The rate of water weight loss is calculated by the following formula: $W=(W_1-W_2)/W_1 \times 100\ \%$, where W_1 is the initial weight and W_2 is the residual weight.

2.14. The tensile strength of skin patches

The tensile properties of samples were investigated by using a universal testing machine. Skin patches were cut into a rectangular shape (10 mm × 40 mm) and measurements were carried out at a loading speed of 5 mm/min and a gauge length of 20 mm. All measurements were performed in quintuplicate.

2.15. Measurements

The morphology of BG and PU-BG was analyzed by using a scanning electron microscope (SEM, S-4800, Hitachi, Japan). The element distribution and quantitative analysis of elements in nanoparticles were characterized by using a SEM accessary energy dispersive spectrometer (EDS) system. The microstructure of BG was tested by using a transmission electron microscope (TEM, JEM-2100F, JEOL, Japan). The mesoporous structure of BG was tested by small-angle X-ray diffraction (SAXRD, D/max 2550 V).

3. Results and discussion

For accelerating wound healing, we aim to couple the BG with specific structured scaffold to obtain multifunctional skin patches. Specially, in order to avoid over-absorbing and maintain moisture balance, we expect to design a hydrophilic/superhydrophilic/hydrophobic structure, where the hydrophilic/superhydrophilic structure exhibits asymmetric wettability, allowing for targeted transport of wound exudate within the material, while simultaneously maintaining a comfortable moist environment due to the hydrophobic layer. For this purpose, we firstly synthesized ions functionalized BG by microfluidics, which was utilized to construct the inner hydrophilic layer in subsequent sections. A three-channel chip was designed to precisely control the flow rate of the Ca^{2+}, Zn^{2+} and Si^{4+}precursor solution (Fig. 2A, Supplementary Fig. S2). The SEM and TEM images reveal that the synthesized BG possessed size uniformity, with a diameter of about 150 nm. (Fig. 2B, Supplementary Fig. S3). We further investigated the effects of the flow rate of Ca^{2+}, Zn^{2+} precursors on the ion content of BG. It is found that the increase of flow rate leads to a significantly larger diameter of BG particles (Supplementary Fig. S4). The element distribution is best illustrated by the EDS mapping analysis, where the Ca^{2+} (purple), Zn^{2+} (yellow) and Si^{4+} (green) ions in BG were more evenly distributed compared with those of BG-1 and BG-2 (Fig. 2C, Supplementary Figs. S5 and S6). Typically, Ca^{2+}, Zn^{2+} and Si^{4+} ions in BG have a weight percentage of 2.03, 3.68 and 29.96 wt%, respectively. The small-angle X-ray diffraction (SAXRD) analysis indicates that the diffraction peak of BG was centered at $2\theta = 1.380^{\circ}$ (Supplementary Fig. S7), which demonstrates an ordered mesostructured[32]. Considering

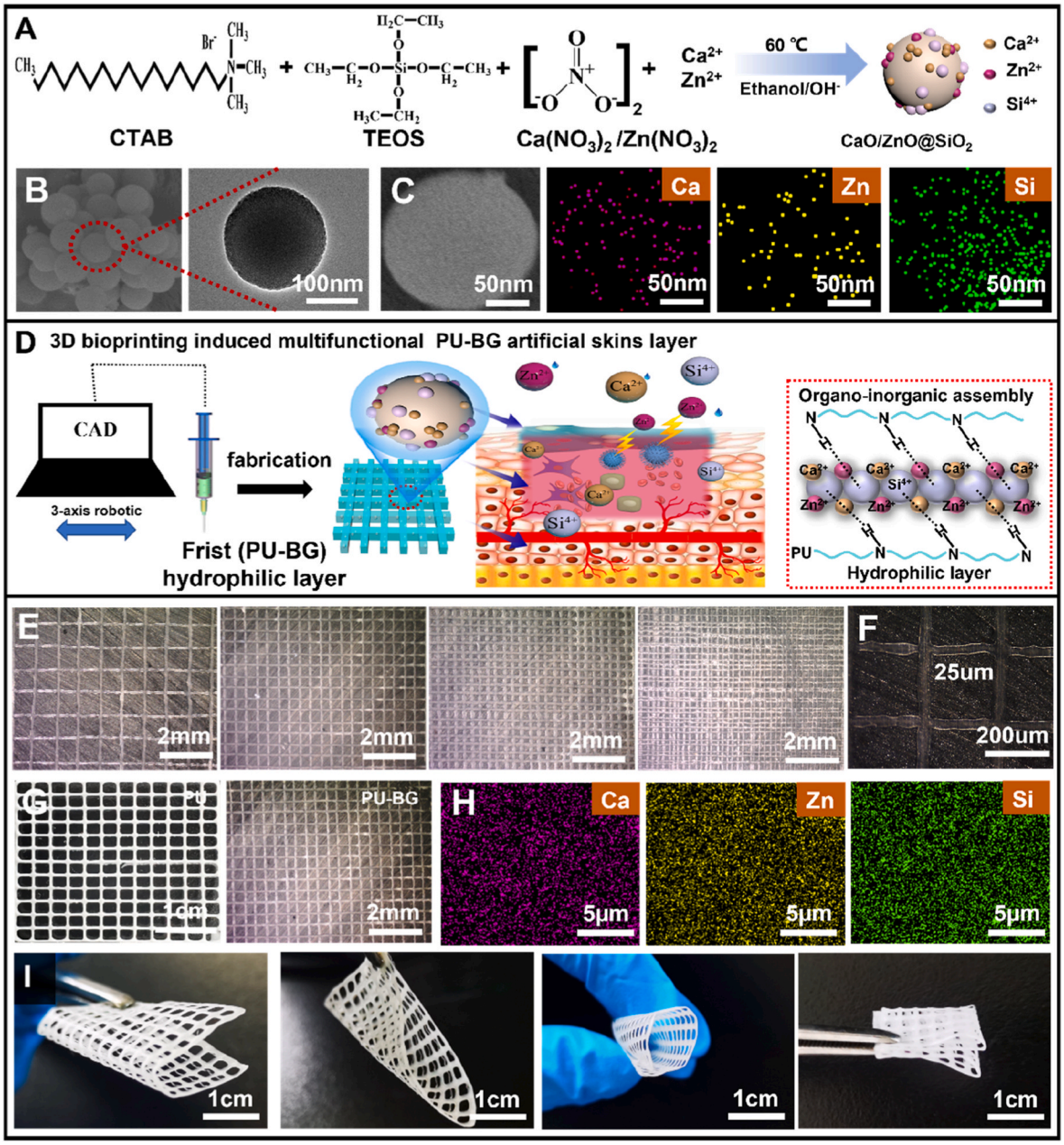

Fig. 2. Fabrication of BG and PU-BG hydrophilic layer. **A**. Schematic illustration of the preparation process of calcium-silica-zinc ions-based BG. **B.** SEM and TEM image of BG. **C.** EDS mapping analysis of the distribution of Ca^{2+}, Zn^{2+} and Si^{4+} ions in BG. **D.** Microfluidic-regulated 3D bioprinting towards precise construction of robust PU-BG hydrophilic layer. **E. F.** Photographs of PU-BG layer with different printing precision, where the smallest accuracy can be up to 25 μm. **G.** Microscope images of the PU and PU-BG layer. **H.** EDS mapping analysis of the distribution of Ca^{2+}, Zn^{2+} and Si^{4+} ions in PU-BG layer. **I.** Photographs demonstrating the outstanding flexibility of the PU-BG layer, which could be bent, coiled and folded.

the high Ca^{2+}, Zn^{2+} and Si^{4+} ions contents, BG was chosen for the following experiments. We then focused on the preparation of the first (PU-BG) layer by MRBP technology (Fig. 2D). Fig. 2E displays the digital micrographs of the varied structures by changing printing precision at different gap ranging from 200 to 1500 μm (Supplementary Fig. S8). As shown in Fig. 2F, the 3D printing accuracy can be up to 25 μm. From the images of PU and PU-BG layer (Fig. 2G, Supplementary Fig. S9), it clearly shows that the 3D printed scaffold exhibits uniform morphology. The EDS mapping analysis proved that the BG are uniformly dispersed in the hydrophilic PU layer (Fig. 2H). In addition, it is found that the diameter distribution of 3D printed scaffold layer varies with the flow rates and chip diameters (Supplementary Figs. S10–11). The flexibility was also evaluated, as shown in Fig. 2I. It can withstand a series of deformations, including bending, coiling and folding, showing excellent flexibility. These results suggest that the MRBP strategy provides a powerful pathway for precise control of microstructure with good reproducibility.

We then focus on the preparation of a tri-layer skin patch, where the second (PU-PAA) super-hydrophilic layer, third (PCL) hydrophobic layer were electrospun in sequence on the PU-BG layer (Supplementary Fig. S12). From the SEM images of PU-PAA and PCL layer (Fig. 3A and B), we can clearly see that the nanofiber scaffold exhibits uniform fiber morphology and the diameter distribution of PU-PAA and PCL layers are centered at 600–1000 nm (Supplementary Fig. S13). The hydrophilic-superhydrophilic-hydrophobic tri-layer structure is verified by the cross-sectional view of the nanofiber scaffold (Supplementary Fig. S14). We then investigated the mechanical strength, flexibility and the permeability of the skin patches to evaluate the applicability as wound

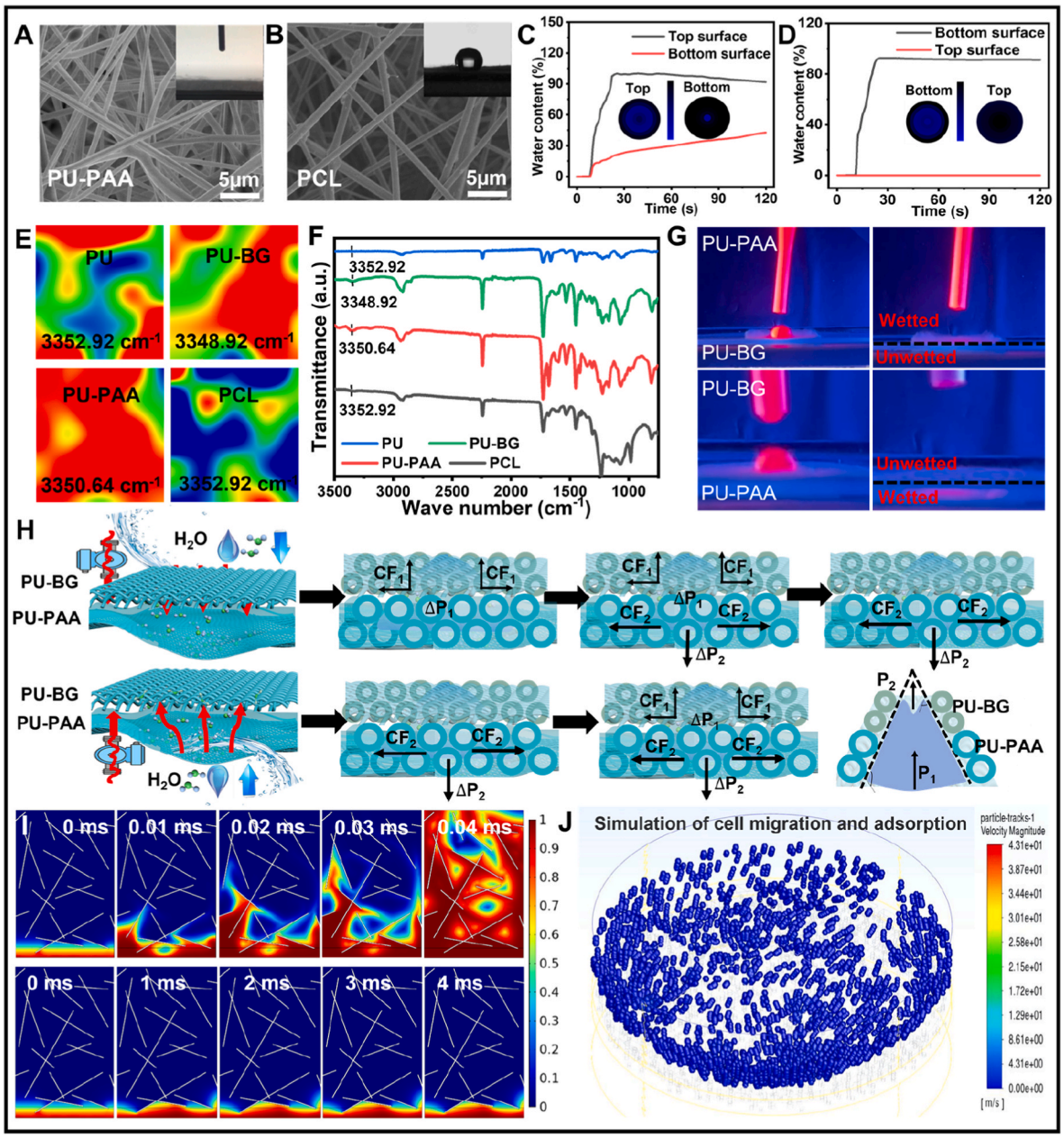

Fig. 3. SEM images of **A.** PU-PAA layer and **B.** PCL layer. **C. D.** MMT results of relative water content of the top and bottom surfaces when the outer and inner layer was facing up, respectively. **E.** Microscopic IR images of PU, PU-BG, PU-PAA and PCL layers. **F.** FT-IR curves of PU, PU-BG, PU-PAA and PCL layers. **G.** Photographs demonstrating the unidirectional fluid draining capability of the self-pumping skin patches. **H.** Diagrams showing the simplified mechanism of the passive wicking process (inset shows the process in the vertical direction). **I.** Theoretical simulation calculation of superhydrophilic layer and hydrophobic layer. **J.** Simulation of cell migration and adsorption.

dressing. The skin patches can exhibit excellent strength from each angle (800 g) and the toughness can be up to 14.5 MPa (Supplementary Figs. S15–16). We measured flexibility of the multilayer skin patches. The results show that the skin patches can withstand a series of deformation, including bending, folding, coiling and stretching (Supplementary Fig. S17). In addition, the tri-layer structure exhibits an air flux of 864.54 m^3/m^2.h.kpa and an average pore size of 3.5 μm (Supplementary Fig. S18). Besides, as the skin patch is used in normal environment, the temperature is not changed dramatically, thus it might have no effect on the performance of the skin patch due to the chemical and biological stability of the chosen materials. Meanwhile, the hydrophobic outer layer can block waters, therefore the performance will not be impacted by the humidity. All these results demonstrate that the tri-layer BG-loaded skin patches show excellent mechanical flexibility, tensile strength and air permeability, which may satisfy the clinical requirements as an ideal artificial skin patch.

To analyze the wettability of each layer and the tri-layer skin patch, contact angle, microscopic infrared and infrared ray (IR) measurements were performed. The contact angle of PU-BG layer changes from 86° to 50° within 14s. This could be attributed to the combination of inorganic bioactive glass with organic fibers, which formed abundant hydrogen bonds and improved the hydrophilicity of the PU layer. For the PU-PAA layer, the microscopic infrared image and IR spectrum indicate abundant of hydrogen bonds at 3350.64 cm^{-1}, which may be due to the formation of hydrogen bonds between the carbonyl oxygen in the PAA and the amino groups of the PU. Experimental results demonstrate that when the PU-PAA layer meets water, it absorbs water immediately, exhibiting super-hydrophilicity, which is consistent with the conjecture.

For PCL layer, its contact angle is 140°, indicating hydrophobility. These results indicate that the skin patches possess a layered wettability (Fig. 3E and F, Supplementary Figs. S19–20). When the skin patch reaches swelling equilibrium in PBS, it expands to about twice of its original volume and increases almost three times of its original weight (Supplementary Fig. S21). More interesting, in virtue of such layered structure, the skin patches are capable of absorbing water rapidly (Supplementary Video S1), which is beneficial for the exudate absorption to avoid the excessive hydration of the wound.

To demonstrate the directional water transportation capabilities of hydrophilicity/superhydrophilicity structure and skin patches, the directional water transport performance tests were implemented. For hydrophilic/superhydrophilic structure, Fig. 3C and D shows the alterations in relative water content when the samples were placed horizontally with brine dripping vertically into the hydrophilicity layer (Fig. 3C) and the superhydrophilicity layer (Fig. 3D). Interestingly, the water content of the PU-BG layer showed slow increase, whereas the water content of the PU-PAA layer increased rapidly to 99 % within 24 s. This phenomenon could be explained by the fact that the enhanced capillary force in the PU-PAA layer stems from the layered multiscale porous structure, effectively drawing water away from the PU-BG layer. In contrast, when the outer layer is oriented downward toward the bottom, the water content of the PU-BG is almost zero, indicating that water cannot penetrate from PU-PAA layer to the PU-BG layer. In addition, the insets in Fig. 3C and D shows dry (dark) and wet (blue) areas on both sides, indicating that water is primarily concentrated in the PU-PAA layer. We then established a simplified physical model with a continuous red quantum dots (QDs) solution by mimicking the exuding wound. In this model, we monitored its dynamic drainage process under UV irradiation. For PU-BG/PU-PAA structure, when contacting PU-BG layer, the droplet of red QDs was pumped through PU-BG layer and wetted PU-PAA layer. Reversely, the droplet wetted PU-PAA layer but was blocked by PU-BG layer when contacting PU-PAA layer (Fig. 3G, Supplementary Fig. S22). Generally, when the droplet comes into contact with the fiber membrane, it enters the capillary channel in the fibers and is subjected to Laplace pressure ($P = 4\gamma \cdot \cos\theta$ D, where γ represents the liquid-gas interfacial tension (the surface tension of water at 25 °C is 0.072 N m^{-1}), θ is the contact angle on the surface of the fibers, and D is the pore size of the fibers). The passive water absorption process of the fiber membrane can be demonstrated by the vertebrae model (Fig. 3H). The variation of the Laplace pressure of a droplet in a capillary is attributed to the difference in water contact angle and pore size between the droplet and the fiber membrane. At the interface, the fluid is subjected to two Laplace pressures, P_1 and P_2, which act in the same direction with an upward-trending Laplace pressure difference $\Delta P_1 = 4\gamma \cdot \cos\theta_2\ D_2 - 4\gamma \cdot \cos\theta_1\ D_1 = P_2 + |P_1|$, where θ_1 represents the water contact angle in the inner layer and θ_2 represents the water contact angle on the transport layer.

Additionally, we investigated the mechanism of cell migration by reducing the flow field to a two-dimensional flow field. We first used CAD software to model the fibres with diameters ranging from 0.6 to 1.2 μm (mostly 0.8–1 μm), which varied in length and showed a heterogeneous and disordered distribution. We then used COMSOL multiphysics field to simulate the absorption properties of the hydrophilic and hydrophobic nanofibre scaffolds and to provide positional maps of the interfaces at different moments. The upper part of the model is set as air (the area with a volume fraction of 0), the upper part of the model is set as blood (the area with a volume fraction of 1), and the interface with a volume fraction of 0.5 is the gas and liquid interface. The fibers in the structure are set as wetted walls with a contact angle θ. The contact angle of hydrophilic fibers is 0°, and the contact angle of hydrophobic fibers is 140°. The bottom edge of the structure is the inlet through which water enters as the liquid moves. The top edge of the structure is the exit. The process of air-liquid interface evolution was calculated by the following equations.

$$\rho^*\partial u/\partial t+\rho(u^*\nabla)u = \nabla\ [-pI+\mu(\nabla u+\nabla u\hat{}T)]+F_{st} + F \quad (1)$$

$$\nabla^*u = 0 \quad (2)$$

where, ρ is the fluid density, u is the fluid velocity, F_{st} indicates the surface tension acting at the interface between the two fluids, F is the volume or body force which acts through the volume of the body.

$$F_{st} = \sigma\delta\kappa n+\delta\nabla s^*\sigma \quad (3)$$

where, σ is the surface tension coefficient (N/m), δ (1/m) is a Dirac delta function on the interface and $\kappa = -\nabla$ n is the curvature, n is the unit normal to the interface, ∇s is the surface gradient operator. From Fig. 3I, for the superhydrophilic nanofiber, we can clearly see that the liquid has completely infiltrated the entire fiber (red part) within 0.04 ms, which is consistent with the contact angle test and shows an extremely excellent absorption performance. For the hydrophobic layer, the simulation time was extended to 4 ms, and the liquid still only covered the surface layer of the fiber and could not be absorbed into the fiber interior. Similarly, we used CAD software for modelling the three-layer scaffold and imported it into ANSYS software for simulation. From Fig. 3j, it is obviously that the periphery and interior of the scaffold adsorb numerous cells (blue part), indicating that the unique asymmetric hydrophilic/superhydrophilic structural structure facilitates cell migration/absorption. Through an in-depth study of microstructure vascular tissue models, the mechanism of cell adsorption and migration is simulated, which provides a theoretical basis for the construction of artificial skin to overcome the arbitrariness in the design of skin patch. This simulation can provide a pre-prediction of the regulation of the transport process at the surface interface of skin patch and is useful for optimizing the selection of materials.

The Ca^{2+}, Zn^{2+} and Si^{4+} ions render the BG with multifunctions, which favor the coagulation function and antibacterial activity, thereby promoting the wound healing process [36,37]. In particular, the ion-release properties of the PU-BG layer are vital. Noteworthy, all the PU layers loaded with different BG contents, no matter high or low, show the same ion-release trend, that is, the ion-release reaches a maximum value within 1 day and keeps almost unchanged with prolonged time (Fig. 4A–C). In addition, it is found that the higher BG content in PU leads to a higher ion-release concentration (Ca^{2+}, Zn^{2+} and Si^{4+} ions). Then, we performed colony and inhibition ring experiments to test the antibacterial capabilities of the PU-BG layer and the skin patches. In the colony experiments (Fig. 4D and E), the colony counts of *E. coli* and *S. aureus* were 1785 ± 67 CFU and 826 ± 33 CFU, after 24 h incubation with PBS, respectively. While for the PU-BG layer, the higher BG content in PU layer shows better antibacterial ability. When the BG content is 3 wt%, the colony counts of *E. coli* and *S. aureus* decreased to 211 ± 22 and 147 ± 13 CFU, respectively. The inhibition ring experiments further confirm the excellent antibacterial ability of the skin patches (Supplementary Fig. S23). In addition, to demonstrate the biocompatibility and cytotoxicity, we selected L929 cells as model cells and incubated them with the PU-BG layer for 24 and 48 h. The fluorescence imaging was used to observe the live/dead cells under calcein AM/PI staining (live cells stained green, dead cells stained red). As shown in Fig. 4F and G, compared to the control group, the biocompatibility of the PU-BG layer slightly declined. The above experimental results indicate that the PU-BG layer possess excellent antibacterial and biocompatibility, which can satisfy the clinical requirements. Specially, the BG content is inversely proportional to the cell viability, that is, higher BG content will lead to a lower survival rate. It is worth noting that even at BG content of 3 wt%, the cell viability can be up to 82.78 and 83.09 % after 24 and 48 h incubation, respectively. Considering the antibacterial and biocompatibility properties, BG content of 3 wt% was chosen for the following experiments.

Excellent adhesive and hemostatic properties are extremely important in the wound healing. We investigated the cell adhesive and

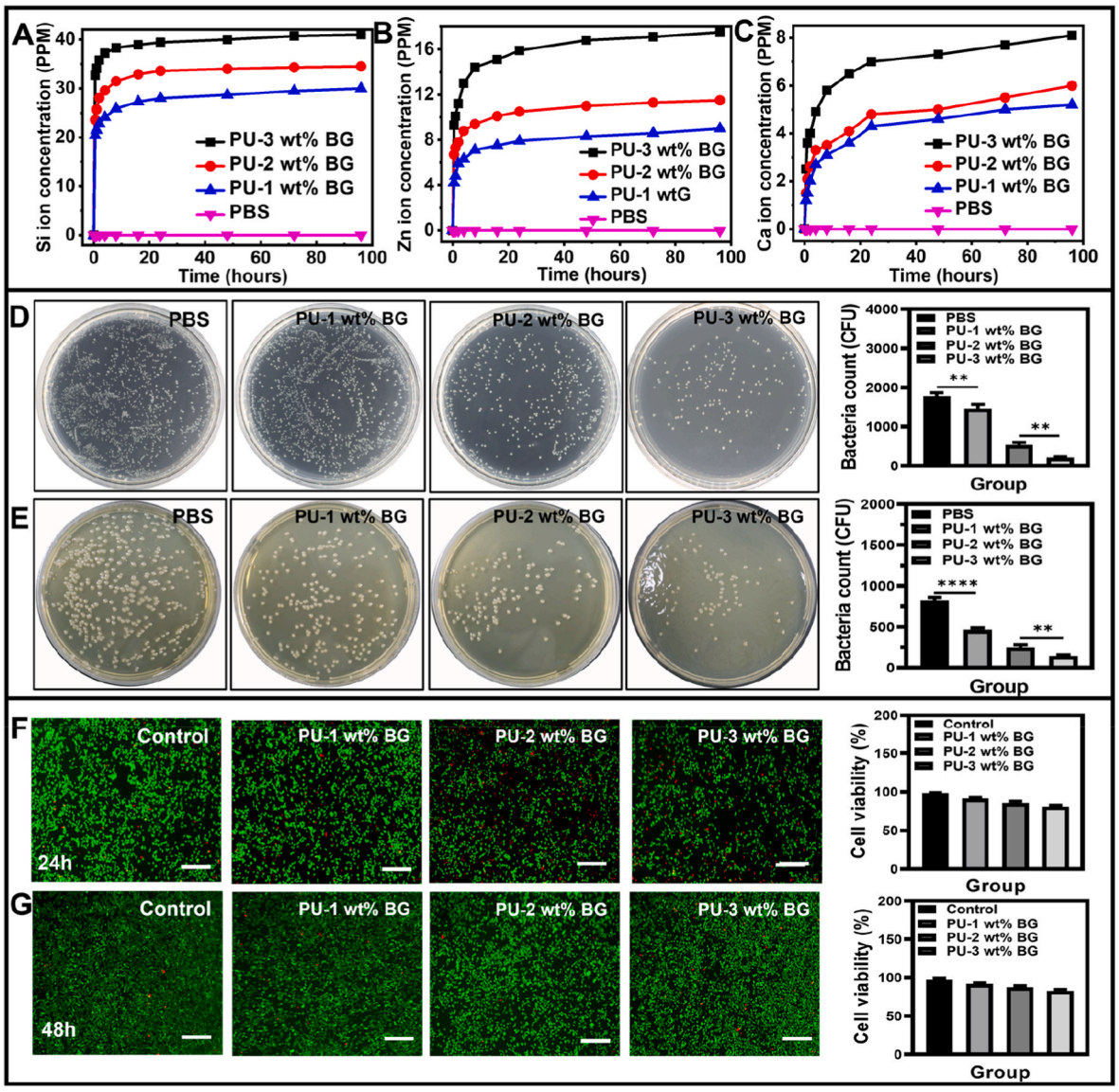

Fig. 4. Anti-bacterial and biocompatible properties of the PU-BG layer. Ion-release property of PU-BG layer in PBS: **A.** Si^{4+} ion, **B.** Zn^{2+} ion and **C.** Ca^{2+} ion. Antibacterial ability of PU-BG layer on agar plates after incubating for 24 h: **D.** *E. coli* and **E.** *S. aureus*. n = 3, **P < 0.01, ****P < 0.0001. Fluorescence images of live/dead cells and cell viability after **F.** 24 and **G.** 48 h incubation with PU-BG layer. Live cells were stained with calcein AM, and dead cells were stained with PI. The scale bar is 100 μm.

migration on the dressing patches. From an in vivo perspective, it is found that the tri-layer skin patches show good cell migration behaviors, which is ascribed to the released ions of the PU-BG layer (Fig. 5A). As clearly indicated in Fig. 5B, the PU-BG/PU-PAA/PCL patch exhibits a higher cell migration ratio than that of the other groups. Specially, the cell migration ratios are 34.3, 50, 59.3 and 85 % for the PBS, PU-BG, PU-PAA and the tri-layer skin patches group, respectively. Hemostasis is the process of forming blood clots. In this case, the nanofibers capture blood cells, platelets and other clotting factors, as well as control the bleeding. The dense fibrous network is beneficial for the platelet adhesion and the released Ca^{2+} ions could promote the generation of thrombin fibrin, which favors the formation of blood clot, enabling the rapid hemostasis. Fig. 5C and D show the hemostasis ability of control, PU-BG, PU-BG/PU-PAA and the BG-loaded tri-layer skin patches in vivo liver bleeding model. Compared with the control group, the tri-layer skin patches show excellent coagulation function with an ultrashort hemostasis time of 3 ± 1 s (hemostasis time of 71 s for the control group). The results indicate that the as-prepared BG-loaded tri-layer skin patches have rapid hemostasis function. This might be attributed to the combined effect of the released Ca^{2+} ions and the tri-layer fiber structure, where the former can effectively stop the bleeding. In addition, the superhydrophilic layer (PU-PAA) might promote the blood capture and cell migration, further intensifying the hemostasis (Fig. 5E and Supplementary Fig. S24).

The second set of experiments was focused on the in vivo study to evaluate the superiority of the tri-layer skin patches. On one hand, the released Zn^{2+}, Ca^{2+} and Si^{4+} ions in the inner layer could effectively kill the bacteria and facilitate clotting. On the other hand, the hydrophilic/superhydrophilic structures can promote cell adhesion and proliferation, wound exudate absorption, and anti-contaminant infection. Therefore, the BG-loaded tri-layer hydrophilic/supehydrophilic skin patches might greatly accelerate the wound healing process (Fig. 6A). To verify our hypothesis, the mouse full-thickness skin defect model was adopted, where a wound area with a diameter of about 2 cm was sliced on the back of a mouse. The tests were given to four groups, namely single layer PU-BG, bilayer PU-BG/PU-PAA, and tri-layer PU-BG/PU-PAA/PCL skin patches, meanwhile the PBS group was as a control. As shown in Fig. 6B, the healing rate of the wounds treated with the tri-layer skin patch is obviously higher than that of the other groups.

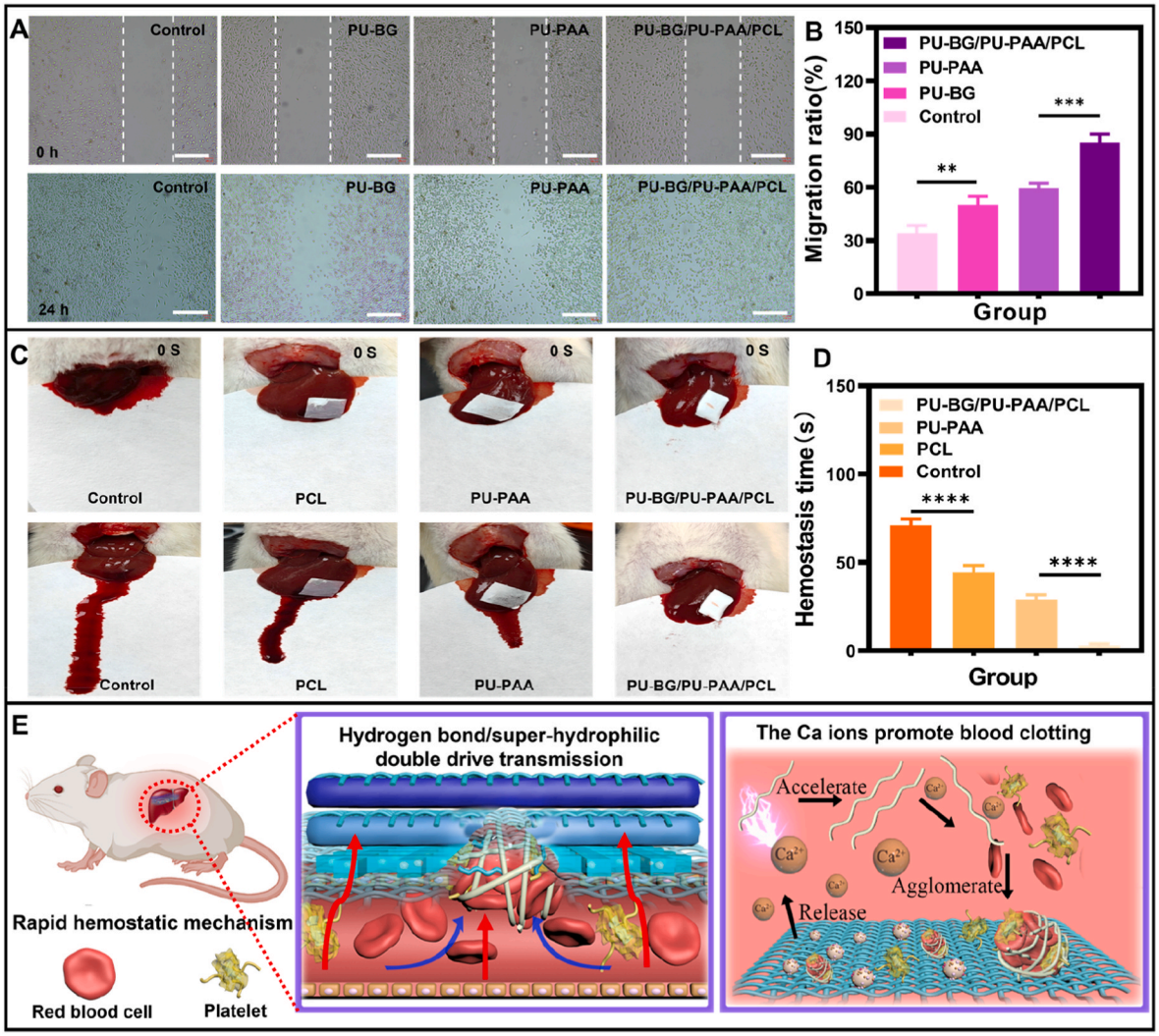

Fig. 5. A. Photographs demonstrate the cell migration of the control, PU-BG, PU-PAA and the PU-BG/PU-PAA/PCL patches. The scale bar is 100 μm. **B.** Quantitative analysis of the cell migration rate. **C.** In vivo liver hemostasis and **D.** corresponding hemostasis time of the control, PCL, PU-PAA and the tri-layer skin patches. n = 3, **P < 0.01, ***P < 0.001, ****P < 0.0001. **E.** Schematic illustration of the wound hemostasis mechanism for the BG-loaded tri-layer skin patches.

Typically, the wound area is 3.3 % for the BG-loaded tri-layer skin patches group, whereas it is 14.3, 9.3 and 8.7 % for the PBS, PU-BG and PU-BG/PU-PAA groups, respectively (Fig. 6D). It should be noted that the wound healing performance of our skin patch is up to 96.7 % at 14 days, which is comparable and even superior to these reported literatures, e.g. 96 % after 18 days of a self-pumping Janus dressing [38], 95.5 % ± 1.0 % at 14 days of thermo-responsive trilayer fibrous dressing [39], 91 % after 14 days of a bioactive composite hydrogel dressing [40].

In addition, the thickness of the wound granulation tissue in mice treated with BG-loaded tri-layer skin patch is 2.39 mm, which is much thicker compared with the other groups: 1.58 mm for PBS group, 2.09 mm for PU/BG group and 2.23 mm for PU-BG/PU-PAA group (Fig. 6C–E). Wound infection also plays a key role in the wound healing process. To investigate the efficacy of the wound dressing in anti-infection, we performed the immunohistochemical analysis of two typical pro-inflammatory factors, interleukin-6 (IL-6) and tumor necrosis factor-α (TNF-α), which occurs in the wound bed. For visually assessing the degree of inflammation in the wound, the IL-6 and TNF-α was stained by immunofluorescence. As seen in Fig. 6F and G, extensive amounts of IL-6 and TNF-α were measured in the control group in PBS solution, indicating a severe inflammatory response. In contrast, very little secretion was observed in the BG loaded tri-layer PU-BG/PU-PAA/PCL skin patch group, which suggests little sign of inflammation or infection formation.

Moreover, angiogenesis is also an important indicator in the wound healing process, and we detected the number of new capillaries by using CD31 immunofluorescence staining. As seen in Fig. 7A, the vascular density of the wound for the skin patch is significantly enhanced, where the relative expression is 3.65 (Fig. 7E). Immunofluorescence staining of collagen was performed to evaluate the collagen deposited granulation tissue (Fig. 7B). It is found that the skin patches group exhibits a higher density distribution of collagen, which is essential for the construction of the extracellular matrix. The relative collagen expression of the skin patches group is 1.68, which is much higher compared with PBS (relative expression of 1), PU-BG (relative expression of 1.29) and PU-BG/PU-PAA groups (relative expression of 1.51) (Fig. 7F). Besides the vascular and collagen density, macrophages, which are classified as early type M1 macrophages and later type M2 macrophages, also play an important role in wound healing. M1-type macrophages secrete pro-inflammatory factors to kill bacteria and anti-inflammatory, while M2-type macrophages can promote tissue regeneration during the regeneration phase. Hence, both the number of M1 macrophages (CD68+/CD86+) and M2 macrophages (CD68+/CD206+) were detected, as shown in Fig. 7C and D. Clearly, the skin patches group shows a lower density distribution of M1-type macrophages (relative expression of

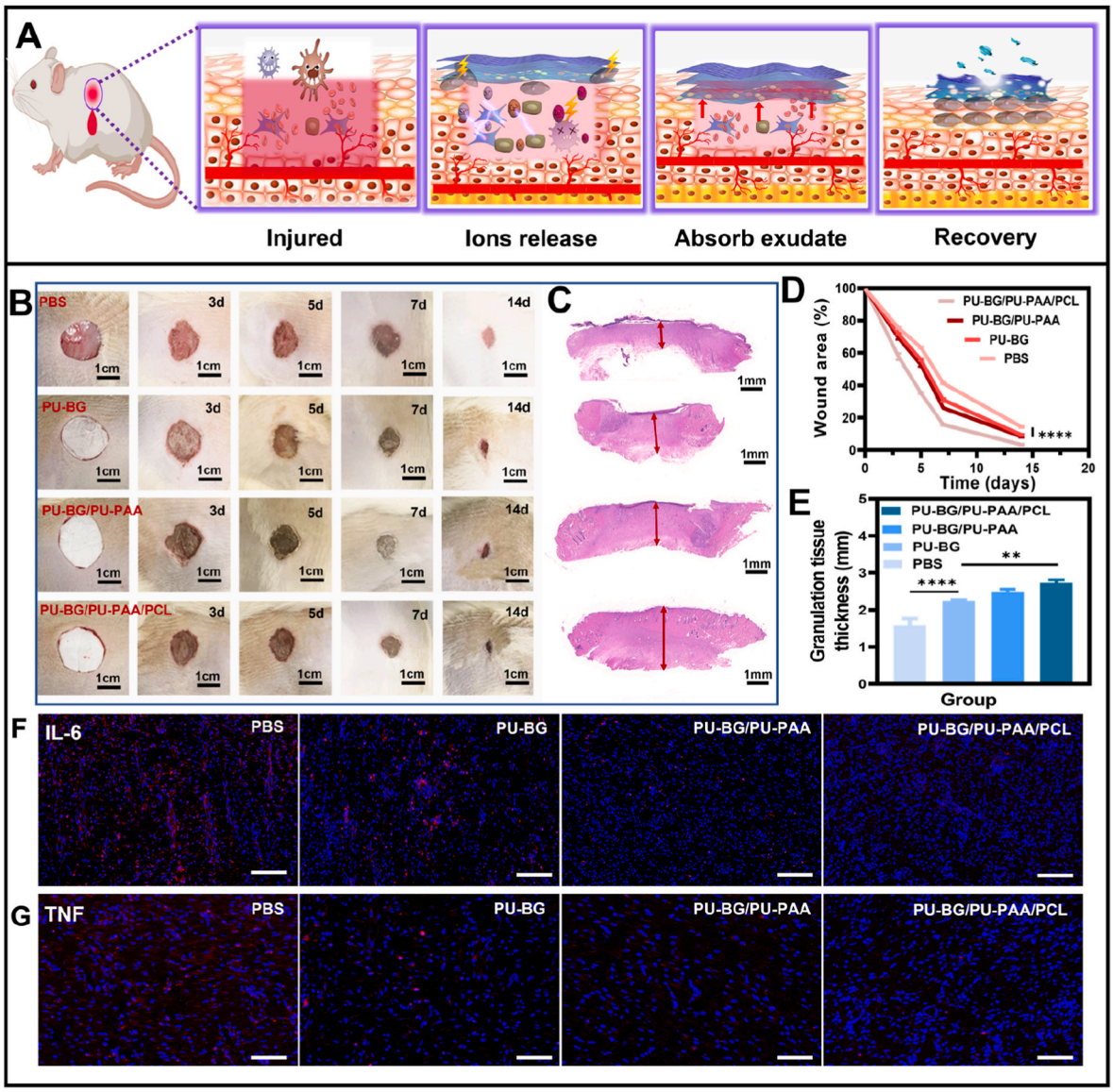

Fig. 6. In vivo wound healing process. A. Schematic illustration of wound healing process. **B.** Digital photographs of the wounds in rats treated with PBS, PU-BG, PU-BG/PU-PAA, and PU-BG/PU-PAA/PCL skin patches at 0, 3, 5, 7, 14 d. **C.** Corresponding microscopy images of granulation growth for the wounds stained by H&E. **D.** Wound area size versus time. **E.** Quantitative analysis of granulation tissue thickness. n = 3, **P < 0.01, ****P < 0.0001. Immunostaining of **F.** IL-6 and **G.** TNF-α in granulation tissues after 7 d. The scale bar is 100 μm.

0.18) in the early wound healing stage (Fig. 7G), indicating slight inflammation. Whereas, the density distribution of M1-type macrophages is higher for the other groups (relative expression, 1.28–0.58), which illustrate severe inflammation. In terms of the later wound healing stage, the M2 macrophages are relatively dense for the skin patches group (Fig. 7D–H), which reveals enhanced tissue regeneration ability. All these in vivo experimental results give strong evidence that the skin patches can effectively promote cell migration, hemostasis, tissue regeneration (vascular and collagen), providing an ideal wound dressing to accelerate wound healing.

Apart from the functions of promoting wound healing and protecting tissues and organs from external bacterial and viral contamination, human skin also shows response ability. To mimic both the physiological and response function, we designed biomedical/electronic difunctional skin patch, consisting of a tactile sensor on the top of a bionic skin layer. It shows greater sensitivity to external changes, demonstrating its potential for pressure sensing. We evaluated the pressure sensing capability by the periodic response, recovery time, and cyclic stability. The relative current response showed distinct behavior under various cyclic stresses. An ideal flexible pressure sensor also should detect tiny changes in pressure. The sensing performance of skin patch was measured under the pressures of P = 100 kPa. For the test, the skin patch was first compressed to a reference pressure, followed by consecutively additional pressures of 100 Pa. It shows that each pressure increment successfully leads to a stepped escalation of the capacitance. Therefore, the minimum resolution achieved is 0.1 % (Supplementary Fig. S26). The step waves under different stress levels demonstrated stable and excellent waveform responses and ultra-wide detection range during compression tests. Compared to other works [41–49], the developed biomedical/electronic difunctional skin patch exhibits a wide pressure detection range of 0–150 kPa, satisfying the requirement in daily human life (Supplementary Fig. S25). To evaluate its cycling stability, the relative current variation during periodic compressing-releasing for 500 cycles was examined. The results reveal its suitability for long-term use (Fig. 8B). In short, as a pressure sensor, the biomedical and electronic dual-function skin patch can achieve excellent sensitivity, and reliable stability for 500 cycles. The relative current variation ($\Delta I/I_0$, $\Delta I = I–I_0$, I and I_0 are the current with and without pressure, respectively) of the

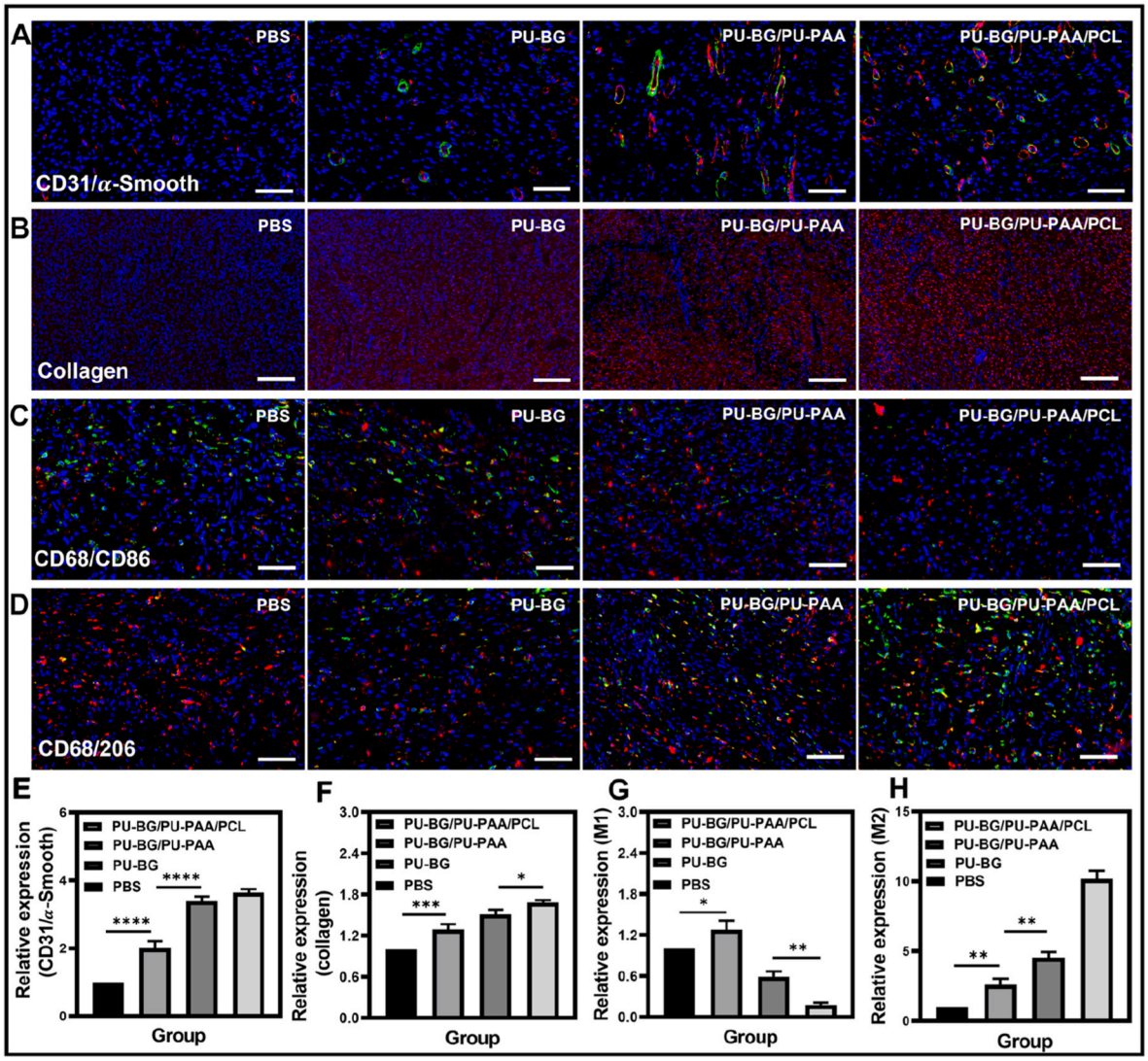

Fig. 7. In vivo study of the skin tissue reconstruction. A. Double immunofluorescence staining of neovascularization. $CD31^+$ structures (red) were surrounded by α-smooth muscle actin positive cells (green), implying vascular ducts. **B.** Immunofluorescence staining of collagen (red). **C. D.** Double immunofluorescence staining of macrophages phenotype markers: $CD68^+$ macrophage (red), $CD86^+$ M1 macrophage (green), and CD206+ M2 macrophage (green) colocalized with DAPI stained nuclei (blue). Quantitative analysis of relative expression of **E.** blood vessels, **F.** collagen, **G.** M1 macrophage and **H.** M2 macrophage. The scale bar is 100 μm. n = 3, *P < 0.05, **P < 0.01, ***P < 0.001, ****P < 0.0001.

pressure sensor in the pressure range of 0–150 kPa was investigated. Here, the pressure sensitivity (S), which is usually defined as $S=(\Delta I/I_0)/P$, is applied to evaluate its sensitivity in different pressure range. As a result, the skin patch possesses four different sensitivities in the sensing range, including 5.87, 2.63, 1.05 and 0.09 kPa^{-1} for the pressure range of 0–3.33, 3.33–18.28, 18.28–46.69 and 46.69–150 kPa, respectively (Supplementary Fig. S27A). Specifically, linearity can reach up to 0.99 in the 0–3.33 kPa range. Compared to other works [41,43,45,49–54], the developed biomedical/electronic difunctional skin patch exhibits excellent sensitivity (Supplementary Fig. S27B). Then the dual-function skin patch sensor was applied in monitoring various human motions and physiological signals. Fig. 8C depicts the resistance response of the movement of pulse signals from the radial artery in the resting state and after exercise. Moreover, we sealed a water container by the skin patch to record the weight loss rate of the water inside, where the water turned into water vapours and produced white mist under solar irradiation. The result indicates that the skin patch possesses excellent air permeability (Supplementary Fig. S28), which is suitable for wearable applications. These results suggest that the resistance change was positively related to the bending degree of the joint, and the biomedical and electronic dual-function skin patch sensor was repeatable and stable.

In order to further investigate the pressure-sensing properties of biomedical/electronic difunctional skin patch, we conducted the real-time monitoring test of human movement (Fig. 9A). When the pressure was pressed slowly and the finger was flexed rapidly, the output signals of the pressure sensors showed significant differences in amplitude and frequency. In addition, the output signals to different body positions (finger, wrist) also showed differences in amplitude at the same frequency of movement (Fig. 9B and C). These devices have great potential for detecting athletic movements with better cyclic stability. Pulse is another physiological signal that reflects the condition of the body. When the patch is attached to the wrist, clear pulse waves can be detected, including percussion (P-wave), tidal (T-wave) and diastolic (D-wave) waves. The regular pulse shape and 72 pulses per minute indicate the health status of the tester (as shown in Fig. 9D and E). From Fig. 9F, it can be seen that the skin patch could be adhered perfectly to the throat due to its good flexibility. The $\Delta R/R_0$ of patch on the throat can be as high as 70 %, which is about 7 times higher (10 %) than that of the finger. Next, we attached the skin patch to the human eyes and neck to

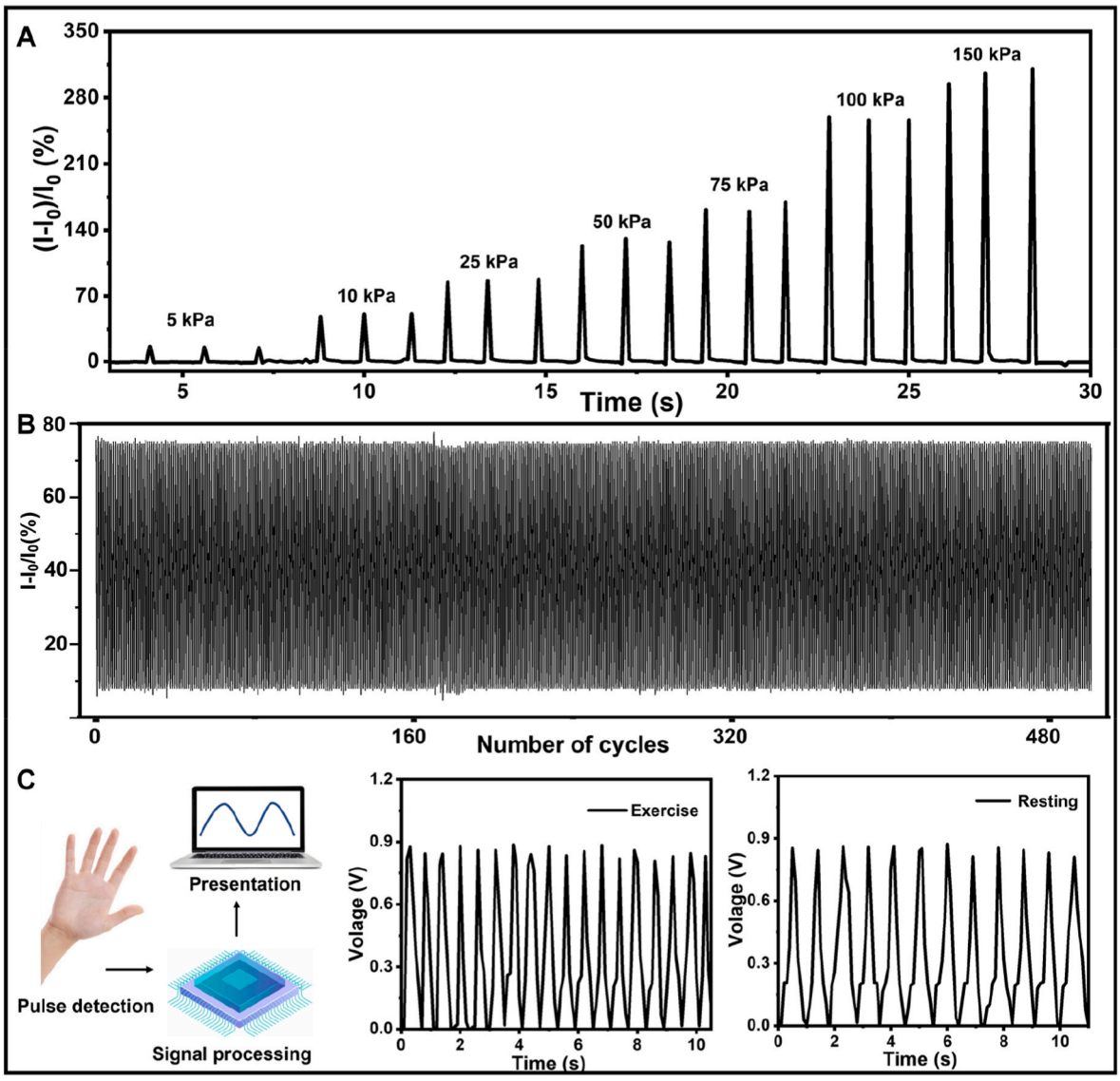

Fig. 8. Compressive properties of the biomedical/electronic dual-functional skin patch as a pressure sensor. A. Relative current variations versus different stress. **B.** Compression-decompression durability test under 10 kPa for 500 cycles. **C.** Schematic illustration and test patterns of the pulse signal detection in the resting state and after exercise.

capture various motion (Fig. 9G–I). During blinking, shaking and nodding of the head, the resistance of the sensing unit showed significant variations. These results indicate that the skin patch shows excellent sensitive properties.

4. Conclusion

In conclusion, we have fabricated biomedical/electronic dual-functional skin patch through MRBP strategy. The skin patch combines both the sensory capability of electronic skin and the therapeutic property of biomedical skin. It is found that the asymmetric structure of the patch could promotes cell adhesion and growth, while it also displays exceptional mechanical properties, antimicrobial activities, hemostasis properties and biological compatibility. The skin patch also enables signal detection, where the sensitivity reached up to 5.87 kPa^{-1} and linearity reached up to 0.99, as well as a wide detection range of 0–150 kPa, high pressure resolution of 0.1 %, exhibiting excellent sensing performance and cyclic stability (over 500 cycles). Crucially, in vivo applications have demonstrated their profound impact on wound healing, showing rapid coagulation, infection prevention, and tissue regrowth. We believe this biomedical/electronic dual-functional skin patch will offer new opportunities for the design and development of skin patch.

Ethics approval and consent to participate

All animal experiments in our study were performed according to the principles of the Declaration of Helsinki, and were approved by the Institutional Animal Care and Use Committee of the Drug Safety Evaluation Center of Jiangsu Province (SYXK(SU)2021–0040).

CRediT authorship contribution statement

Ting Dong: Writing – original draft. **Jie Hu:** Data curation. **Yue Dong:** Investigation. **Ziyi Yu:** Formal analysis. **Chang Liu:** Investigation. **Gefei Wang:** Validation, Methodology. **Su Chen:** Writing – review & editing, Project administration, Methodology, Formal analysis.

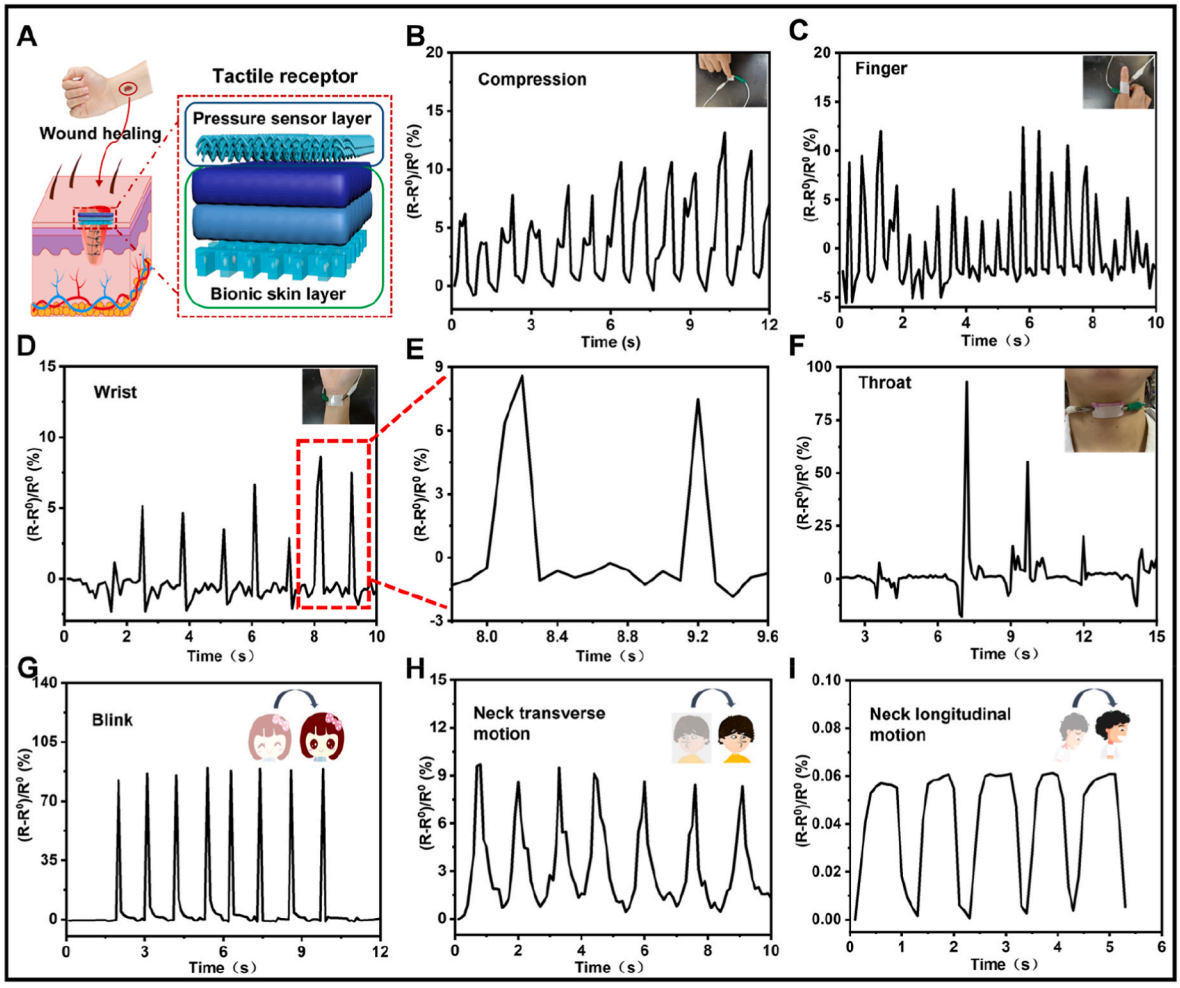

Fig. 9. Detection of subtle and violent human movements. **A.** Schematic illustration of the human tactile receptors. **B.** Detection of compression signal. **C.** Detection of bending signal attached to the finger. **D.** Detection of pulse signal attached to the wrist. **E.** Magnified image of a single pulse. **F.** Detection of swallowing signals attached to the throat. (Inset) Tester attached to the finger, wrist, and throat. Resistance responses of the composite materials during (**G**) blink process, (**H**) neck transverse movements and (**I**) longitudinal movements.

Declaration of competing interest

The authors declare no competing interests.

Acknowledgements

This work was supported by National Natural Science Foundation of China (22278225, 82170581,22308160), Natural Science Foundation of Jiangsu Province (BK20211133, BK20230327), the Postgraduate Research & Practice Innovation Program of Jiangsu Province (KYCX23_1471), and Priority Academic Program Development of Jiangsu Higher Education Institutions (PAPD).

Appendix A. Supplementary data

Supplementary data to this article can be found online at https://doi.org/10.1016/j.bioactmat.2024.06.015.

References

[1] B.S. Kim, S. Das, J. Jang, D. Cho, Decellularized extracellular matrix-based bioinks for engineering tissue- and organ-specific microenvironments, Chem. Rev. 120 (19) (2020) 10608–10661, https://doi.org/10.1021/acs.chemrev.9b00808.

[2] Y. Cao, Y.J. Tan, S. Li, W.L. Wang, H. Guo, Y. Cai, C. Wang, B.C.-K. Tee, Self-healing electronic skins for aquatic environments, Nature Electronics 2 (2019) 75–82, https://doi.org/10.1038/s41928-019-0206-5.

[3] I. You, D.G. Mackanic, N. Matsuhisa, J. Kang, J. Kwon, L. Beker, J. Mun, W. Suh, T. Y. Kim, J.B.-H. Tok, Z. Bao, U. Jeong, Artificial multimodal receptors based on ion relaxation dynamics, Science 370 (6519) (2020) 961–965, https://doi.org/10.1126/science.aba5132.

[4] M.A. Darabi, A. Khosrozadeh, R. Mbeleck, Y. Liu, Q. Chang, J. Jiang, J. Cai, Q. Wang, G. Luo, M. Xing, Skin-inspired multifunctional autonomic-intrinsic conductive self-healing hydrogels withpressure sensitivity, stretchability, and 3D printability, Adv. Mater. 30 (4) (2018) 1–8, https://doi.org/10.1002/adma.201705922.

[5] Z. Liu, Y. Wang, Y. Ren, G. Jin, C. Zhang, W. Chen, Poly(ionic liquid) hydrogel-based anti-freezing ionic skin for a soft robotic gripper, Mater. Horiz. 7 (2020) 919–927, https://doi.org/10.1039/c9mh01688k.

[6] J. Zhu, H. Zhou, E.M. Gerhard, S. Zhang, F.I.P. Rodríguez, T. Pan, H. Yang, Y. Lin, J. Yang, H. Cheng, Smart bioadhesives for wound healing and closure, Bioact. Mater. 19 (2023) 360–375, https://doi.org/10.1016/j.bioactmat.2022.04.020.

[7] J.E. Hyun, T. Lim, S.H. Kim, J.H. Lee, Wearable ion gel based pressure sensor with high sensitivity and ultra-wide sensing range for human motion detection, Chem. Eng. J. 484 (149464) (2024) 1385–8947, https://doi.org/10.1016/j.cej.2024.149464.

[8] M. Won, G. Oh, H. Lee, J. Kim, D.-S. Kim, Humidity sensors based on cellulose nanofiber fabricated on a three-dimensional (3D) curved surface, Nanomaterials 13 (23) (2023) 3005, https://doi.org/10.3390/nano13233005.

[9] C. Zhang, H. Chen, X. Ding, F. Lorestani, C. Huang, B. Zhang, B. Zheng, J. Wang, H. Cheng, Y. Xu, Human motion-driven self-powered stretchable sensing platform based on laser-induced graphene foams, Appl. Phys. Rev. 9 (2022) 011413, https://doi.org/10.1063/5.0077667.

[10] Y. Peng, J. Zhou, Y. Yang, J.-C. Lai, Y. Ye, Y. Cui, An Integrated 3D hydrophilicity/hydrophobicity design for artificial sweating skin (i-TRANS) mimicking human body perspiration, Adv. Mater. 34 (44) (2022) 2204168, https://doi.org/10.1002/adma.202204168.

[11] M.M. De Santis, H.N. Alsafadi, S. Tas, D.A. Bölükbas, S. Prithiviraj, I.A.N. Da Silva, M. Mittendorfer, C. Ota, J. Stegmayr, F. Daoud, M. Königshoff, K. Swärd, J.

A. Wood, M. Tassieri, P.E. Bourgine, S. Lindstedt, S. Mohlin, D.E. Wagner, Extracellular-matrix-reinforced bioinks for 3D bioprinting human tissue, Adv. Mater. 33 (3) (2021) 2005476, https://doi.org/10.1002/adma.202005476.
[12] L. Zhou, A.C. Wolfes, Y. Li, D.C.W. Chan, H. Ko, F.G. Szele, H. Bayley, Lipid-bilayer-supported 3D printing of human cerebral cortex cells reveals developmental interactions, Adv. Mater. 32 (31) (2020) 2002183, https://doi.org/10.1002/adma.202002183.
[13] L. Gao, M.E. Kupfer, J.P. Jung, L. Yang, P. Zhang, Y.D. Sie, Q. Tran, V. Ajeti, B. T. Freeman, V.G. Fast, P.J. Campagnola, B.M. Ogle, J. Zhang, Myocardial tissue engineering with cells derived from human-induced pluripotent stem cells and a native-like, high-resolution, 3-dimensionally printed scaffold, Circ. Res. 120 (2017) 1318–1325, https://doi.org/10.1161/CIRCRESAHA.116.310277.
[14] A. Lee, A.R. Hudson, D.J. Shiwarski, J.W. Tashman, T.J. Hinton, S. Yerneni, J. M. Bliley, P.G. Campbell, A.W. Feinberg, 3D bioprinting of collagen to rebuild components of the human heart, Science 365 (2019) 482–487, https://doi.org/10.1126/science.aav9051.
[15] L.Y. Daikuara, X. Chen, Z. Yue, D. Skropeta, F.M. Wood, M.W. Fear, G.G. Wallace, 3D bioprinting constructs to facilitate skin regeneration, Adv. Funct. Mater. 32 (3) (2022) 2105080, https://doi.org/10.1002/adfm.202105080.
[16] H. Zhao, J. Xu, H. Yuan, E. Zhang, N. Dai, Z. Gao, Y. Huang, F. Lv, L. Liu, Q. Gu, S. Wang, 3D printing of artificial skin patches with bioactive and optically active polymer materials for anti-infection and augmenting wound repair, Mater. Horiz. 9 (1) (2022) 342–349, https://doi.org/10.1039/d1mh00508a.
[17] Y. Wang, W. Huang, L. Ren, X. Chen, Y. Ke, Fabrication and characterization of a PAM modified PHBV/BG scaffold, Chin. Sci. Bull. 54 (2009) 2940–2946, https://doi.org/10.1007/s11434-009-0263-7.
[18] L. Wang, Q. Yang, M. Huo, D. Lu, Y. Gao, Y. Chen, H. Xu, Engineering single-atomic iron-catalyst-integrated 3D-printed bioscaffolds for osteosarcoma destruction with antibacterial and bone defect regeneration bioactivity, Adv. Mater. 33 (31) (2021) 2100150, https://doi.org/10.1002/adma.202100150.
[19] R.D. Farahani, M. Dubé, D. Therriault, Three-dimensional printing of multifunctional nanocomposites: manufacturing techniques and applications, Adv. Mater. 28 (28) (2016) 5794–5821, https://doi.org/10.1002/adma.201506215.
[20] Q. Lin, X. Hou, C. Ke, Ring shuttling controls macroscopic motion in a three-dimensional printed polyrotaxane monolith, Angew. Chem. 129 (16) (2017) 4523–4528, https://doi.org/10.1002/anie.201612440.
[21] F.V. Ferreira, C.G. Otoni, K.J.D. France, H.S. Barud, L.M.F. Lona, E.D. Cranston, O. J. Rojas, Porous nanocellulose gels and foams: breakthrough status in the development of scaffolds for tissue engineering, Mater. Today 37 (2020) 126–141, https://doi.org/10.1016/j.mattod.2020.03.003.
[22] Z. Lei, P. Wu, A supramolecular biomimetic skin combining a wide spectrum of mechanical properties and multiple sensory capabilities, Nat. Commun. 9 (2018) 1134, https://doi.org/10.1038/s41467-018-03456-w.
[23] B. Xue, H. Sheng, Y. Li, L. Li, W. Di, Z. Xu, L. Ma, X. Wang, H. Jiang, M. Qin, Z. Yan, Q. Jiang, J.-M. Liu, W. Wang, Y. Cao, Stretchable and self-healable hydrogel artificial skin, Natl. Sci. Rev. 9 (2022) 147, https://doi.org/10.1093/nsr/nwab147.
[24] C. Cai, X. Zhang, Y. Li, X. Liu, S. Wang, M. Lu, X. Yan, L. Deng, S. Liu, F. Wang, C. Fan, Self-healing hydrogel embodied with macrophage-regulation and responsive-gene-silencing properties for synergistic prevention of peritendinous adhesion, Adv. Mater. 34 (5) (2022) 2106564, https://doi.org/10.1002/adma.202106564.
[25] S. Pandey, M. Mahato, P. Srinath, U. Bhutani, T.J. Goap, P. Ravipati, P.K. Vemula, Intermittent scavenging of storage lesion from stored red blood cells by electrospun nanofibrous sheets enhances their quality and shelf-life, Nat. Commun. 13 (2022) 7394, https://doi.org/10.1038/s41467-022-35269-3.
[26] Y. Wang, Y. Xu, W. Zhai, Z. Zhang, Y. Liu, S. Cheng, H. Zhang, In-situ growth of robust superlubricated nano-skin on electrospun nanofibers for post-operative adhesion prevention, Nat. Commun. 13 (2022) 5056, https://doi.org/10.1038/s41467-022-32804-0.
[27] T. Cui, J. Yu, Q. Li, C.-F. Wang, S. Chen, W. Li, G. Wang, Large-scale fabrication of robust artificial skins from a biodegradable sealant-loaded nanofiber scaffold to skin tissue via microfluidic blow-spinning, Adv. Mater. 32 (32) (2020) 2000982, https://doi.org/10.1002/adma.202000982.
[28] L. Shi, X. Liu, W. Wang, L. Jiang, S. Wang, A self-pumping dressing for draining excessive biofluid around wounds, Adv. Mater. 31 (5) (2018) 1804187, https://doi.org/10.1002/adma.201804187.
[29] X. Zhou, J. Liu, W. Liu, W. Steffen, H.-J. Butt, Fabrication of stretchable superamphiphobic surfaces with deformation-induced rearrangeable structures, Adv. Mater. 34 (2022) 2107901, https://doi.org/10.1002/adma.202107901.
[30] S. Qian, J. Wang, Z. Liu, J. Mao, B. Zhao, X. Mao, L. Zhang, L. Cheng, Y. Zhang, X. Sun, W. Cui, Secretory fluid-aggregated janus electrospun short fiber scaffold for wound healing, Small 18 (2022) 2200799, https://doi.org/10.1002/smll.202200799.
[31] F. Bao, G. Pei, Z. Wu, H. Zhuang, Z. Zhang, Z. Huan, C. Wu, J. Chang, Bioactive self-pumping composite wound dressings with micropore array modified janus membrane for enhanced diabetic wound healing, Adv. Funct. Mater. 30 (49) (2020) 2005422, https://doi.org/10.1002/adfm.202005422.
[32] Z. Zhang, W. Li, Y. Liu, Z. Yang, L. Ma, H. Zhuang, E. Wang, C. Wu, Z. Huan, F. Guo, J. Chang, Design of a biofluid-absorbing bioactive sandwich-structured Zn–Si bioceramic composite wound dressing for hair follicle regeneration and skin burn wound healing, Bioactive Mater. 6 (7) (2021) 1910–1920, https://doi.org/10.1016/j.bioactmat.2020.12.006.
[33] C. Achille, C. Parra-Cabrera, R. Dochy, H. Ordutowski, A. Piovesan, P. Piron, L. V. Looy, S. Kushwaha, D. Reynaerts, P. Verboven, B. Nicolaï, J. Lammertyn, D. Spasic, R. Ameloot, 3D printing of monolithic capillarity-driven microfluidic devices for diagnostics, Adv. Mater. 33 (25) (2021) 2008712, https://doi.org/10.1002/adma.202008712.
[34] A. Vartanian, Pinpoint 3D printing, Nat. Rev. Mater. 7 (2022) 336, https://doi.org/10.1038/s41578-022-00445-w.
[35] X. Zhang, H. Fu, X. Liu, A. Yao, D. Wang, W. Huang, Y. Zhao, X. Jiang, In vitro bioactivity and cytocompatibility of porous scaffolds of bioactive borosilicate glasses, Chin. Sci. Bull. 54 (2009) 3181–3186, https://doi.org/10.1007/s11434-009-0275-3.
[36] Y. Zhang, M. Chang, F. Bao, M. Xing, E. Wang, Q. Xu, Z. Huan, F. Guo, J. Chang, Multifunctional Zn doped hollow mesoporous silica/polycaprolactone electrospun membranes with enhanced hair follicle regeneration and antibacterial activity for wound healing, Nanoscale 11 (2019) 6315–6333, https://doi.org/10.1039/c8nr09818b.
[37] Z. Zhang, Q. Dai, Y. Zhang, H. Zhuang, E. Wang, Q. Xu, L. Ma, C. Wu, Z. Huan, F. Guo, J. Chang, Design of a multifunctional biomaterial inspired by ancient Chinese medicine for hair regeneration in burned skin, ACS Appl. Mater. Interfaces 12 (11) (2020) 12489–12499, https://doi.org/10.1021/acsami.9b22769.
[38] L. Zhou, F. Liu, J. You, B. Zhou, W. Guo, W. Qu, X. Ren, G. Gao, A novel self-pumping janus dressing for promoting wound immunomodulation and diabetic wound healing, Adv. Healthcare Mater. 13 (2024) 2303460, https://doi.org/10.1002/adhm.202303460.
[39] Z. Qiu, Y. Gao, D. Qi, M. Wu, Z. Mao, J. Wu, Thermo-responsive trilayered fibrous dressing with liquid gate for dynamical exudate regulation and wound moisture balance, Adv. Funct. Mater. 34 (2024) 2311997, https://doi.org/10.1002/adfm.202311997.
[40] S. Shang, K. Zhuang, J. Chen, M. Zhang, S. Jiang, W. Li, A bioactive composite hydrogel dressing that promotes healing of both acute and chronic diabetic skin wounds, Bioact. Mater. 34 (2024) 298–310, https://doi.org/10.1016/j.bioactmat.2023.12.026.
[41] Y. Zheng, R. Yin, Y. Zhao, H. Liu, D. Zhang, X. Shi, B. Zhang, C. Liu, C. Shen, Conductive MXene/cotton fabric based pressure sensor with both high sensitivity and wide sensing range for human motion detection and E-skin, Chem. Eng. J. 420 (2021) 127720, https://doi.org/10.1016/j.cej.2020.127720.
[42] Y. Wang, M. Zhu, X. Wei, J. Yu, Z. Li, B. Ding, A dual-mode electronic skin textile for pressure and temperature sensing, Chem. Eng. J. 425 (2021) 130599, https://doi.org/10.1016/j.cej.2021.130599.
[43] W. Hu, D. Song, X. Shi, L. Zhou, Z. Zhao, T. Xue, X. Lin, N. Liu, Anisotropic Electronic Skin for Neurofeedback, Advance Functional Materials, 2023 2309395, https://doi.org/10.1002/adfm.202309359.
[44] C. Chen, J.-L. Xu, Q. Wang, X.-L. Li, F.-Q. Xu, Y.-C. Gao, Y.-B. Zhu, H.-A. Wu, J.-W. Liu, Biomimetic multimodal receptors for ComprehensiveArtificial human somatosensory system, Adv. Mater. (2024) 2313228, https://doi.org/10.1002/adma.202313228.
[45] L. Wu, X. Li, J. Choi, Z.-J. Zhao, L. Qian, B. Yu, I. Par, Beetle-Inspired gradient slant structures for CapacitivePressure sensor with a broad linear response range, Adv. Funct. Mater. (2024) 2312370, https://doi.org/10.1002/adfm.202312370.
[46] J. Seong, B.-U. Bak, D. Lee, J. Jin, J. Kim, Tribo-piezoelectric synergistic $BaTiO_3$/PDMS micropyramidal structure for high-performance energy harvester and high-sensitivity tactile sensing, Nano Energy 122 (2024) 109264, https://doi.org/10.1016/j.nanoen.2024.109264.
[47] J. Zou, Y. Ma, C. Liu, Y. Xie, X. Dai, X. Li, S. Li, S. Peng, Y. Yue, S. Wang, C.-W. Nan, X. Zhang, Self-powered sensor based on compressible ionic gelelectrolyte for simultaneous determination of temperatureand pressure, InfoMat (2024) e12545, https://doi.org/10.1002/inf2.12545.
[48] Z. Ding, W. Li, W. Wang, Z. Zhao, Y. Zhu, B. Hou, L. Zhu, M. Chen, L. Che, Highly sensitive iontronic pressure sensor withSide-by-Side package based on alveoli and arch structure, Adv. Sci. (2024) 2309407, https://doi.org/10.1002/advs.202309407.
[49] X. Wang, J. Zi, Y. Chen, Q. Wu, Z. Xiang, Y. Tu, P. Yang, Y. Wan, Multistage microstructured ionic skin for real-time VitalSigns monitoring and human-machine interaction, Energy Environment Materials 0 (2024) e12767, https://doi.org/10.1002/eem2.12767.
[50] M.-J. Yin, Z. Yin, Y. Zhang, Q. Zheng, A.P. Zhang, Micropatterned elastic ionic polyacrylamide hydrogel for low-voltage capacitive and organic thin-film transistor pressure sensors, Nano Energy 58 (2019) 96–104, https://doi.org/10.1016/j.nanoen.2019.01.032.
[51] Y. Zheng, T. Lin, N. Zhao, C. Huang, W. Chen, G. Xue, Y. Wang, C. Teng, X. Wang, D. Zhou, Highly sensitive electronic skin with a linear response based on the strategy of controlling the contact area, Nano Energy 85 (2021) 106013, https://doi.org/10.1016/j.nanoen.2021.106013.
[52] C. Zhao, Y. Fang, H. Chen, S. Zhang, Y. Wan, M.S. Riaz, Z. Zhang, W. Dong, L. Diao, D. Ren, F. Huang, ACS Nano 17 (5) (2023) 4862–4870, https://doi.org/10.1021/acsnano.2c11564.
[53] P. Lu, L. Wan, P. Zhu, J. Huang, Y. Wang, N. Bai, Y. Wang, G. Li, J. Yang, K. Xie, J. Zhang, B. Yu, Y. Dai, C.F. Guo, Iontronic pressure sensor with high sensitivity and linear response over a wide pressure range based on soft micropillared electrodes, Sci. Bull. 11 15 (2021) 1091–1100, https://doi.org/10.1016/j.scib.2021.02.019.
[54] Y. Lee, J. Myoung, S. Cho, J. Park, J. Kim, H. Lee, Y. Lee, S. Lee, C. Baig, H. Ko, Bioinspired gradient conductivity and stiffness for ultrasensitive electronic skins, ACS Nano 1 (2021) 1795–1804, https://doi.org/10.1021/acsnano.0c09581.